A new computational approach to microwave heating of two-phase porous materials

D.D. Dinčov
Harrow School of Computer Science, University of Westminster, Harrow, UK
K.A. Parrott and K.A. Pericleous
School of Computing and Mathematical Sciences, University of Greenwich, London, UK

Received April 2002
Revised October 2003
Accepted December 2003

Keywords *Microwaves, Porous materials, Electromagnetic radiation*

Abstract *Computational results for the microwave heating of a porous material are presented in this paper. Combined finite difference time domain and finite volume methods were used to solve equations that describe the electromagnetic field and heat and mass transfer in porous media. The coupling between the two schemes is through a change in dielectric properties which were assumed to be dependent on both temperature and moisture content. The model was able to reflect the evolution of both temperature and moisture fields as well as energy penetration as the moisture in the porous medium evaporates. Moisture movement results from internal pressure gradients produced by the internal heating and phase change.*

1. Introduction

Microwave heating has the ability to penetrate and heat from within the product. Other advantages over the conventional means of heating include energy efficiency, lack of combustion products and a quick start-up period. Industrial applications of microwaves include removing moisture from porous materials such as drying of textiles, wood, paper and ceramics. In medicine they are used for thawing frozen tissue, warming blood, and tumor therapies (Saltiel and Datta, 1999).

The largest consumer of microwave power is the food industry where its applications include: baking, blanching, cooking, dehydration, drying, pasteurization, sterilization, etc.

Microwave heating produces moisture distributions that are complex and fundamentally different from convective heating. Moisture loss occurs through evaporation, diffusion and pressure driven flow (where the flow/heating dynamics allow internal pressure build-up to occur) and directly affects food quality. Uneven heating, e.g. at edges, will increase moisture loss as well as leading to nutrient loss and flavour degradation (Ni *et al.*, 1999).

Although there is a large literature on microwave food processing (Datta and Anantheswaran, 2001; Saltiel and Datta, 1999) most of the published work has considered either the detailed electromagnetic field distribution in microwave ovens with given effective conductivities (Fu and Metaxas, 1994) or detailed heat and mass transfer (usually diffusion driven but sometimes pressure driven) in biomaterials with assumed electromagnetic field distributions (Datta and Anantheswaran, 2001; Zhou *et al.*, 1994). However, electric permittivities and effective conductivities are highly sensitive to moisture concentration so that moisture transport has a direct effect on the

International Journal of Numerical Methods for Heat & Fluid Flow
Vol. 14 No. 6, 2004
pp. 783-802

0961-5539
DOI 10.1108/09615530410544319

microwave power distribution and a fully coupled approach is essential to further progress. Perré and Turner (1999) have shown that solving a combined "Maxwell-Heat and Mass Transfer" model is feasible for the microwave drying of timber though demanding both computationally and in terms of numerical accuracy. Our approach has followed that of Turner but for reasons of computational economy we have chosen to incorporate a time domain Maxwell solver within a general-purpose multi phase CFD solver in order to apply this methodology to food processing.

The CFD computations make use of a multi phase porous media flow model with phase change for the moisture transport (Ni *et al.*, 1999; Saltiel and Datta, 1999) in the food material. Local (pressure and temperature dependent) saturation conditions are applied at each computational cell interface to model evaporation and re-condensation. The solution domain for the CFD calculations is defined by the food material and packaging. Surface boundary conditions can be used to allow for heat transfer by forced convention, radiation and evaporation.

With internal heat generation the mechanism mass transfer is primarily through a total pressure gradient established due to the rapid vapour generation inside the sample. Most of the moisture is vapourized before leaving the sample. However, when the sample is initially very wet and the pressure inside the sample rises rapidly, liquid may be removed from the sample under the influence of internal pressure gradients (Lyins and Hatcher, 1972).

The temperature and moisture distributions in a material during microwave heating are influenced by the interaction and absorption of radiation by the medium and the accompanying transport processes due to the dissipation of electrical energy into heat (Metaxas and Meredith, 1983). Factors that determine how an object will heat when subjected to microwave radiation include: the geometry of the cavity in which heating takes place (Saltiel and Datta, 1999), the geometry and size of the object (Chamchong and Datta, 1999) and its electromagnetic and thermal parameters (Chamchong and Datta, 1999; Metaxas and Meredith, 1983).

2. Electromagnetic field in microwave enclosures

The distribution of electromagnetic fields in space and time is governed by Maxwell's equations (Yee, 1966). The differential form of Maxwell's equations can be expressed in terms of the electric field intensity $\mathbf{E}$ and the magnetic field density $\mathbf{H}$

$$\nabla \times \mathbf{E} = -\frac{\partial(\mu \mathbf{H})}{\partial t} \tag{1}$$

$$\nabla \times \mathbf{H} = \sigma_{\text{eff}} \mathbf{E} + \frac{\partial(\varepsilon \mathbf{H})}{\partial t} \tag{2}$$

$$\nabla \cdot (\varepsilon \mathbf{E}) = \rho \tag{3}$$

$$\nabla \cdot \mathbf{H} = 0 \tag{4}$$

where $\varepsilon = \varepsilon_0 \varepsilon_{\text{r}}'$ is the permittivity ($\varepsilon_0 = 8.85 \times 10^{12}$ F/m is the permittivity of free space), μ is the permeability and ε_{r}' is the relative permittivity. The effective conductivity σ_{eff} is related to the relative loss factor $\varepsilon_{\text{eff}}''$ for the material by

$$\sigma_{\text{eff}} = \omega \varepsilon_0 \varepsilon''_{\text{eff}} \tag{5}$$

where $\omega = 2\pi f$ is the angular frequency, $\varepsilon''_{\text{eff}}$ is made up from contributions from dipolar, electronic, atomic, space charge and conduction losses (Saltiel and Datta, 1999).

The dielectric properties of materials subjected to microwave heating play a key role in designing proper microwave applicators. Both ε'_{r} and $\varepsilon''_{\text{eff}}$ are temperature (T) dependent and a number of investigations have been made in order to define this behaviour (Ayappa *et al.*, 1991; Metaxas and Meredith, 1983). In most cases, their values increase as the material thaws and thereafter decrease as the temperature increases. Their variation for temperatures up to the boiling point is relatively small (Metaxas and Meredith, 1983). Most foodstuffs contain an appreciable amount of water so the variation of ε'_{r} and $\varepsilon''_{\text{eff}}$ with the moisture content can be more significant.

Losses under the influence of the magnetic field can be described in a similar way to losses in electric materials. However, most materials used in microwave processing are magnetically transparent. The magnetic permeability in this work is assumed to have the value of the free space permeability $\mu_0 = 4\pi \times 10^{-7}\,\text{H/m}$.

An electromagnetic wave impinging on a lossy food surface will be exponentially attenuated, through absorption of energy. Penetration depth, defined as the distance from the surface where the power of the wave has decreased to $1/e$ of the surface value, can be approximated by the following expression (Saltiel and Datta, 1999):

$$d = \frac{\lambda_0}{2\pi(2\varepsilon'_{\text{r}})^{1/2}} \left[\left(1 + \left(\frac{\varepsilon''_{\text{eff}}}{\varepsilon'_{\text{r}}} \right)^2 \right)^{1/2} - 1 \right]^{-1/2} \tag{6}$$

where λ_0 is the wavelength of the incident radiation in free space.

2.1 Boundary conditions

In the presence of highly conducting material interfaces, the tangential magnetic field and the tangential electric field should disappear. If both media have finite conductivity and there are no sources at the interface, then boundary/interface conditions for tangential electric and magnetic fields along the interface are, i.e.

$$(\mathbf{E}_2 - \mathbf{E}_1) \times \mathbf{n} = 0 \tag{7}$$

$$(\mathbf{H}_2 - \mathbf{H}_1) \times \mathbf{n} = 0 \tag{8}$$

where $\mathbf{n}$ represents the unit normal vector to the interface.

3. Finite-difference time domain scheme

The electromagnetic solver used in this work is based on the finite-difference time domain method (FDTD) (Yee, 1966). This is the most computationally efficient of the three related numerical methods in use as time domain solvers in high-frequency electromagnetic computations: edge elements, FDTD and the co-volume method. First-order edge elements provide more geometric flexibility but their accuracy for wave propagation is disappointing on unstructured meshes in 3D (Monk and Parrott, 2001). The co-volume method is a generalisation of FDTD to unstructured meshes. Its mathematical structure is very close to edge elements and so it would be expected to give similar accuracy on a given

mesh. FDTD gives much better accuracy, for a similar number of degrees of freedom when structured meshes are acceptable (Monk, 1996; Monk and Suli, 1994). Domestic microwave ovens are usually rectangular enclosures so structured meshes can provide an adequate approximation to the microwave cavity geometry. Sub-structured meshing in the FDTD solver can be adopted to allow for general food geometry and still retain wave propagation accuracy (Monk and Parrott, 2001; Živanovic, *et al.*, 1991) and this will be the basis for future work on more realistic geometries.

In summary, FDTD is second-order accurate in both time and space on uniform and non-uniform meshes, and can be locally refined without significant loss of accuracy. The use of (semi)-structured meshes ensures optimally fast computations for the most time-consuming component of the overall calculations and it is sufficient for our geometric modelling requirements. The FDTD discretisation is composed of a number of finite volumes, as shown in Figure 1. It makes use of finite difference approximations to electric and magnetic fields components, that are staggered both in time and space. E and H field components are positioned at half-step intervals around unit volumes and they are evaluated at alternate half-time steps, effectively giving centered difference expressions for both time and space derivatives.

Values for ε and σ are specified at cell centres as $\varepsilon(i, j, k)$ and $\sigma(i, j, k)$. Continuity across any interface of the tangential electric fields is implemented automatically since we aligned the mesh with the interface.

4. Heat and mass transfer in porous media

4.1 Dissipated power

The dissipated power density is the microwave energy absorbed by the material. It is eventually converted into thermal energy. The dissipated power density is influenced

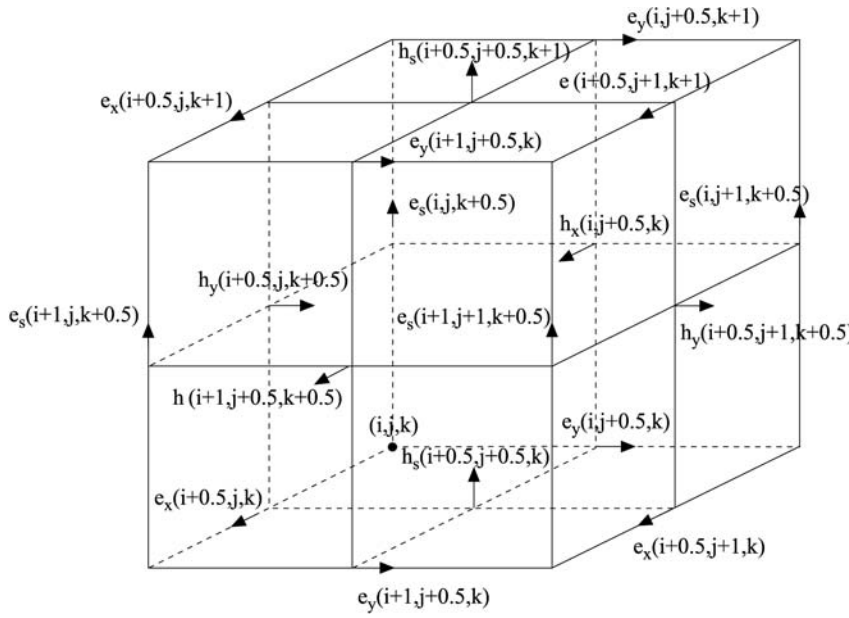

Figure 1.
Yee scheme nodal description

by the field intensity distribution and electric properties. The heating function, Q, which will be included as a source term in the heat transfer equation, can be expressed as (Metaxas and Meredith, 1983):

$$Q = \omega\varepsilon_0\varepsilon''_{\text{eff}}|\mathbf{E}|^2 + \omega\mu_0\mu''_{\text{eff}}|\mathbf{H}|^2. \tag{9}$$

In the case of dielectric materials, there are no magnetic losses and the second term on the right-hand side of equation (9) is negligible.

Microwave devises use time harmonic sources. The time variations of $\mathbf{E}$ in a sinusoidal cycle are extremely fast (on order less than 10^{-11} s) and there is little reason to follow such quick changes, especially since the characteristic thermal time scales are many orders of magnitude larger. Consequently, the volumetric heating rate can be computed from peak field amplitudes as:

$$Q = \frac{1}{2}\sigma_{\text{eff}}|E_{\max}|^2. \tag{10}$$

4.2 Heat transfer equations

There are two energy transfer equations within the processed specimen each corresponding to one "phase". The first phase consists of solid and liquid and the second one is the gas phase:

$$\bar{\rho}_{\text{sl}}\frac{\partial H_{\text{sl}}}{\partial t} + \nabla\cdot\left(\bar{\rho}_{\text{sl}}\mathbf{u}_{\text{l}}\frac{C_{\text{pl}}}{\overline{C}_{\text{psl}}}H_{\text{sl}} - \bar{k}_{\text{sl}}\nabla T_{\text{sl}}\right) = Q + S_{\text{sl}}^{\text{int}} \tag{11}$$

$$\bar{\rho}_{\text{g}}\frac{\partial H_{\text{g}}}{\partial t} + \nabla\cdot(\bar{\rho}_{\text{g}}\mathbf{u}_{\text{g}}H_{\text{g}} - \bar{k}_{\text{g}}\nabla T_{\text{g}}) = S_{\text{g}}^{\text{int}} \tag{12}$$

where the thermal conductivity k is averaged for each phase as follows:

$$\bar{k}_{\text{sl}} = (1-\phi)k_{\text{s}} + \phi M k_{\text{l}} \tag{13}$$

$$\bar{k}_{\text{g}} = \phi(1-M)k_{\text{g}} \tag{14}$$

Specific heat C_{p} and density ρ are averaged similarly. The heating function is included in the solid-liquid heat transfer equation. There will be an interphase transfer between the two phases, represented by the interface source S_i^{int} defined as:

$$S_i^{\text{int}} = h_{ij}A_{\text{s}}\left(H_i^{\text{int}} - H_i\right) \tag{15}$$

where h_{ij} is a bulk-to interface heat transfer coefficient, A_{s} the total interface area and H^{int} the interface enthalpy.

4.3 Mass transfer equations

Gas phase continuity equation is given by:

$$\frac{\partial(\rho_{\text{g}}r_{\text{g}})}{\partial t} + \nabla\cdot(\rho_{\text{g}}r_{\text{g}}\mathbf{u}_{\text{g}}) = \dot{m}. \tag{16}$$

and the 1iquid phase continuity equation by:

$$\frac{\partial(\rho_l r_l)}{\partial t} + \nabla \cdot (\rho_l r_l \mathbf{u}_l) + \dot{m} = 0. \tag{17}$$

where r_g and r_l are gas and liquid volume fractions, respectively. The interface mass transfer rate $\dot{m}$ is determined from the balance of heat through the interface between the phases (Ishii, 1975):

$$\dot{m} = \frac{h_1^m \left(H_1^{int} - H_1\right) + h_2^m \left(H_2^{int} - H_2\right)}{H_1^{int} - H_2^{int}} \tag{18}$$

where h_1^m and h_2^m are bulk-to interface mass transfer coefficients.

4.4 Darcy's law

Darcy's law can be used to represent momentum transfer in the porous medium. For liquid it can be expressed in the form:

$$\mathbf{u}_l = -\frac{K_l}{\lambda_l}(\nabla P_g + l_r \nabla r_l + l_T \nabla T) \tag{19}$$

where $l_r = -\partial P_c(r_l, T)/\partial r_l$ and $l_T = -\partial P_c(r_l, T)/\partial T$ are terms related to capillary pressure P_c. Also K_l and λ_l denote the permeability tensor and the liquid viscosity, respectively, and P_g gas pressure.

The appropriate version of Darcy's law for the gas phase is

$$\mathbf{u}_g = -\frac{K_g}{\lambda_g}(\nabla P_g) \tag{20}$$

where K_g and λ_g are the permeability tensor and the liquid viscosity, respectively.

5. Finite volume method

The finite volume (FV) method is almost universally used in problems involving fluid flow with heat and mass transfer. Consequently, there are many FV codes readily available to use in the microwave heating problem, both commercial and public-domain. In the work presented, the PHOENICS code (2002) was chosen:

(1) for its ability to handle the two-fluid (water-vapour) transport using the IPSA (Spalding, 1981) algorithm; and

(2) for the facility for easy insertion of user Fortran routines to handle the physics of the problem and the coupling with the electro-magnetically induced heat source.

Only the salient features of the FV method affecting this application will be described here, since full descriptions can be readily found elsewhere (Patankar, 1980).

The transport equations for all conserved variables Φ, in a multiphase system, may be cast in a universal form as follows:

$$\frac{\partial(\rho_i r_i \Phi)}{\partial t} + \mathrm{div}(\rho_i r_i u_i \Phi - \Gamma_k r_i \,\mathrm{grad}(\Phi)) = S_\Phi + S_{IP} \tag{21}$$

The RHS contains volumetric source terms within each phase S_Φ and inter-phase transport terms S_{IP}. The subscript i refers to each individual phase.

The resulting system is then solved numerically by iteration.

To discretise equation (21), a computational grid restricted to the porous biomaterial is first constructed. In PHOENICS, the grid is structured (although it can be Cartesian, cylindrical polar, or body-fitted) and it can be non-uniform. Equation (21) is then integrated over each grid cell volume, for each variable Φ, with the variable placed in the centre of the cell. This leads to the FV transport equation,

$$\Phi_p = \left(\sum_{j=e,w,n,s,h,l} (a_j \Phi_j) + a_t \Phi_{\text{old}} + (S_\Phi + S_{\text{IP}})_p V_p \right) \Big/ \sum_{j=e,w,n,s,h,l} (a_j) + a_t \qquad (22)$$

The convection and diffusion terms of equation (21) are converted by this integration into cell-face fluxes, which are contained in the influence coefficients a_j. The cell value of the variable Φ_p is then related to all its space (e, w, n, s, h, l) and time t neighbours through these influence coefficients. For numerical stability the source terms are usually split into two parts by liberalization (Patankar, 1980). A positive part of the source then appears in the denominator.

Solution of equation (22) is obtained by iteration within each time step, using a variant of the SIMPLE (Patankar, 1980, Spalding, 1981) pressure correction scheme, which inks continuity errors to iterative pressure adjustments in each cell. To prevent checkerboard type solutions, PHOENICS staggers the velocity variables in each coordinate direction, so that the cell-face flux is coincident to the appropriate velocity component. Since the electrically induced heat sources will vary during the computation as moisture levels and temperature vary in the biomaterial, the FDTD code is called at suitable time intervals.

6. Solution technique

The coupling algorithm is shown in Figure 2 and is similar to that of Perré and Turner (1999). It makes use of the fact that the electromagnetic field distribution microwave oven responds to changes in the dielectric properties of the biomaterial on a timescale that is very small compared with the thermal process. It can be summarized as follows: the FDTD solver is run until the steady-state (pure-time harmonic) is sufficiently well approximated and the power distribution Q, computed from the peak field amplitudes, has converged. The temperature distribution and moisture content are then evolved according to this power distribution until the electrical properties of the medium have changed significantly. The electromagnetic solver is then rerun, until a new steady-state is reached. The whole procedure is repeated until the required heating time is reached. There are many possible criteria that could be used to determine when the electromagnetic field components have converged. However, the key quantity linking the two models is the microwave heating function Q. This heating function was determined at each FDTD time step and the total sum over the biomaterial calculated i.e.

$$I^n = \int_V \mathrm{d}V = \frac{1}{2} \sum_{i,j,k} \sigma_{i,j,k} \left| E^{\max}_{i,j,k} \right|^2 \Delta x_i \Delta y_j \Delta z_k. \qquad (23)$$

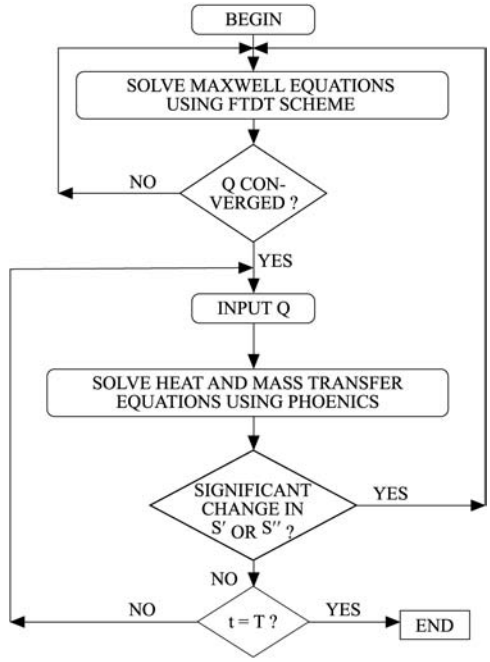

Figure 2.
Coupling algorithm

The relative change in the total sum was used as a measure of the convergence of the FDTD scheme to the time-harmonic state.

The cavity and the waveguide are meshed for the FDTD computation with a tensor-product cartesian mesh, but only the biomaterial needs to be meshed for the heat and mass transfer calculations within PHOENICS. Since the two meshes are independent, a transfer function (conserving the total Q for the biomaterial) is used to map the heating function Q from the FDTD mesh to the heat and mass transfer mesh. The time step for the electromagnetic solver is limited by the stability condition (Yee, 1966)

$$\Delta t < \frac{c}{\sqrt{\Delta x^{-2} + \Delta y^{-2} + \Delta z^{-2}}} \tag{24}$$

where $c = (\varepsilon\mu)^{-1/2}$ is the local electromagnetic wave speed (however, an unconditionally stable ADI version of FDTD has recently been developed (Zheng *et al.*, 2000)). The time step was set to be 95 per cent of the minimum time step for the mesh and material.

7. Model description

The microwave oven model used in this paper consists of a simple waveguide and cavity containing a block of porous material of rectangular cross section, as shown in Figure 3. A waveguide attached to the centre of one of the cavity faces is used to deliver the excitation field. The input plane of the waveguide is excited in the dominant TE^{z}_{10} mode with an amplitude of $E_0 = 100\,\mathrm{kV/m}$. The source operates at the domestic

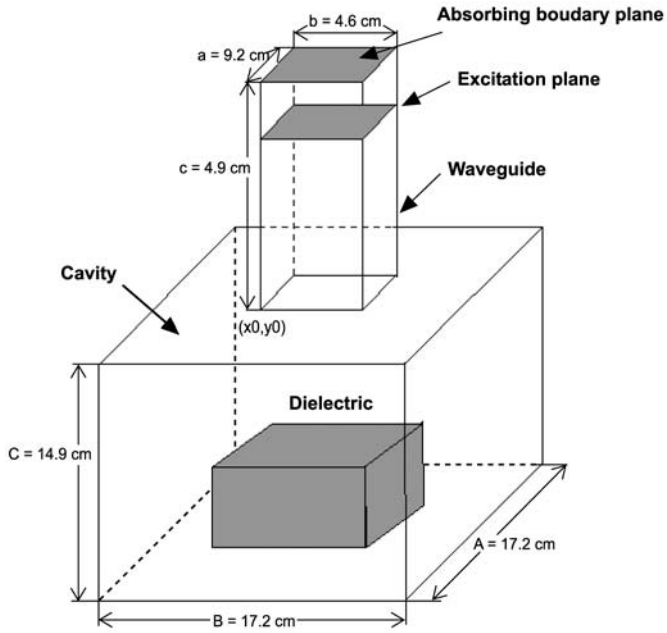

Figure 3.
Microwave oven model

microwave frequency of 2.45 GHz and is located away from the junction, so that the higher order modes are virtually non-existent. The energy which is reflected back due to a mismatch between the impedance of the waveguide and that of the cavity passes through the excitation plane, which appears transparent, to the absorbing boundary.

The amplitudes of the incident wave are given by:

$$E_y^{\text{inc}} = E_0 \sin\left(\frac{\pi(x - x_0)}{A}\right) \cos(\omega t - \beta z_{k0}) \tag{25}$$

$$H_x^{\text{inc}} = \frac{E_0 \beta}{\omega \mu} \sin\left(\frac{\pi(x - x_0)}{A}\right) \cos(\omega t - \beta z_{k0-1/2}) \tag{26}$$

where x_0, y_0 are the coordinates of the waveguide corner, $z = z_{k0}$ is the excitation plane (three mesh intervals away from the absorbing boundary in our model), A is the waveguide x-dimension and β is the mode wave number.

If the solid, liquid and gaseous phase temperature dependencies are known, then the porous medium relative permittivity and loss factor can be calculated using a simple homogenization (Perré and Turner, 1999):

$$\bar{\varepsilon}(M, T) = (1 - \phi)\varepsilon_s(T) + \phi(M\varepsilon_l(T) + (1 - M)\varepsilon_g(T)) \tag{27}$$

where M is the fractional moisture content and ϕ the porosity. The dielectric permittivity and dielectric loss for dried solid were deduced from the permittivity of 80 per cent moist reconstituted potato starch on $T = 20$°C (Bengtsson and Ohlsson, 1974) using equation (27). The temperature dependencies of water and gas were taken from

literature (Metaxas and Meredith, 1983). Using these expressions in equation (6) allows the calculation of the penetration depth of this porous biomaterial and its variation with moisture for a range of temperatures shown in Figure 4. The fluid movement through the porous media is governed by the permeability for gas (k_g) and water (k_w). These are calculated using two different intrinsic permeabilities k_{gi} and k_{wi} (Table I) for gas and water that take into account the structural changes occurring during the microwave process (Ni *et al.*, 1999), i.e. $k_g = k_{gi}k_{gr}$, $k_w = k_{wi}k_{wr}$ where the relative permeabilities k_{gr} and k_{wr} are used to interpolate between the dry and fully saturated end points (Bear, 1998):

$$k_{gr} = 1 - 1.1S_w \quad S_w < 1/1.1,$$

$$k_{gr} = 0 \quad S_w > 1/1.1,$$

$$k_{wr} = \left(\frac{S_w - S_{ir}}{1 - S_{ir}}\right)^3 \quad S_w > S_{ir},$$

$$k_{wr} = 0 \quad S_w < S_{ir},$$

where S_{ir} is the irreducible liquid saturation. Above two equations are shown graphically in Figure 5, using the values given in Table I.

7.1 Initial and boundary conditions

The general boundary condition on the material's surface can be expressed as:

$$-k\frac{\partial T}{\partial n} = h_c(T_s - T_a) + \sigma_{rad}\varepsilon_{rad}\left(T_s^4 - T_a^4\right) - \dot{m}L \tag{28}$$

where T_s is the load surface temperature, T_a is the convective air temperature, n represents the normal to the surface, h_c is the convective heat transfer coefficient, σ_{rad} is the Stefan-Boltzmann constant, ε_{rad} is the radiative surface emissivity and L is the

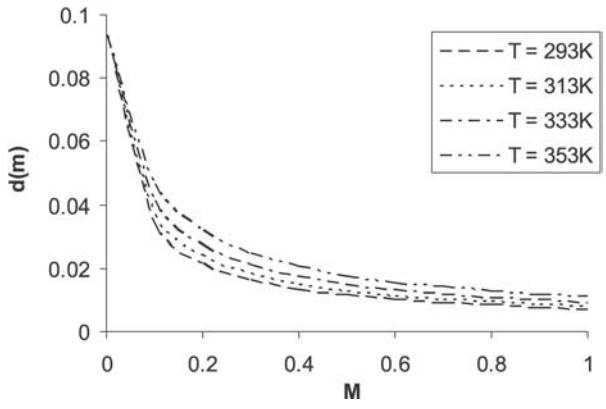

Figure 4.
Penetration depth

Parameter	Value	Source
Porosity, ϕ	0.55	
Initial saturation, S_w	0.80	
Irreducible saturation, S_{ir}	0.08	Bear (1998)
Intrinsic gas permeability at very dry state, k_{gi} (m^2)	10×10^{-14}	Ni *et al.* (1999)
Intrinsic liquid permeability at very wet state, k_{wi} (m^2)	5×10^{-14}	Ni *et al.* (1999)
Initial temperature, T_{init}(℃)	20	This work
Surrounding air temperature, T_{init} (℃)	20	This work
Specific heat of gas, c_{pg} (J/kg/K)	1,005	
Specific heat of water, c_{pw} (J/kg/K)	4,180	
Specific heat of potato, c_{ps} (J/kg/K)	3,500	
Gas density, ρ_g (kg/m^3)	1.189	
Water density, ρ_w (kg/m^3)	1000	
Potato density, ρ_s (kg/m^3)	1050	
Dynamic viscosity of gas, μ_g (Pa s)	1.8×10^{-5}	
Dynamic viscosity of water, μ_w (Pa s)	5.468×10^{-4}	
Latent heat of vapourisation, L(J/kg)	2.435×10^{6}	
Convective heat transfer coefficient, h($W/m^2/K$)	10	Ma *et al.* (1995)
Thermal conductivity of gas, k_g (W/m/K)	0.0258	
Thermal conductivity of water, k_l (W/m/K)	0.597	
Thermal conductivity of potato, k_s (W/m/K)	0.6	

Table I.
Input parameters used in the computations

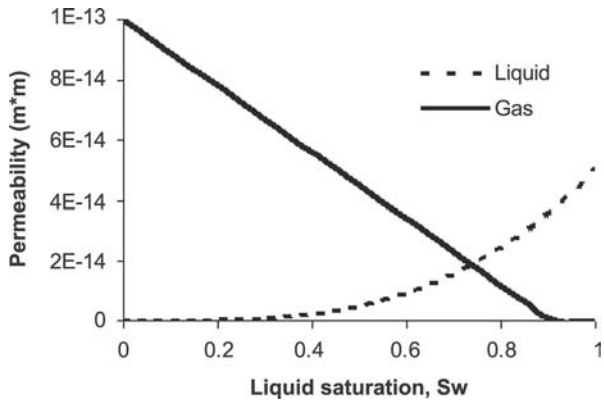

Figure 5.
Relative permeabilities

latent heat of vaporisation of the evaporated liquid. The first term in the equation represents the natural convection by which the load is cooled. The second term is the surface radiation and is important as a cooling mechanism at high load temperatures, or as a heating mechanism if susceptors are used. Since materials with a high moisture content are being observed in this study, the last term, evaporative cooling will have the strongest impact on the temperature profile. The boundary condition for the pressure on the material's surface is simply $P_g = P_{atm}$.

The initial conditions for the example considered here are $P_g(t = 0) = P_{atm}$, $T(t = 0) = T_{init}$.

8. Model validation

In order to validate our method, the combined algorithm was used to calculate the temperature distribution considering the same geometry and mesh as detailed by Ma *et al.* (1995). The workload in the oven is a phantom gel placed in the PTFE container to maintain shape. The dielectric properties are assumed to be temperature dependent only and were measured experimentally. The load and the cavity have rectangular cross sections and energy is supplied to the cavity by a rectangular waveguide excited at a dominant TE_{10} mode (Figure 3). The power dissipated in the experiment was estimated to be approximately 600 W and consequently, the applied excitation amplitude was evaluated from the temperature rise to closely apply to the experiment. Other gel parameters used are: specific heat $C_p = 3,600\,\mathrm{J/kg/K}$, density $\rho = 1,000\,\mathrm{kg/m^3}$ and thermal conductivity $k = 0.55\,\mathrm{J/K/m/s}$. The initial temperature of the load was $T_{init} = 5°\mathrm{C}$ and ambient temperature chosen was $T_{amb} = 30°\mathrm{C}$.

The program was run for a period of 180 s and temperature was measured across the horizontal and vertical planes of symmetry. The calculated power distribution in the horizontal plane of symmetry is shown in Figure 6. It is almost identical to the one that was obtained by Ma *et al.* (1995). The calculated temperature after 180 s in the horizontal and vertical plane of symmetry are shown in Figures 7 and 8, respectively. They are compared to the experimentally measured distributions (Ma *et al.*, 1995) (Figures 9 and 10). It can be seen that in both planes the agreement is very good. However, there is a displacement in measured temperatures in Figures 9 and 10 due to the fact that the biomaterial was placed in a container. The main patterns of the temperature distribution have been successfully predicted. In particular, the hot spots along the centre of the front face of the load and at the corners. Because the oven is asymmetric, the position of the hot spot on the face is not in

Figure 6.
Calculated power distribution, $Q(\mathrm{W/m^3})$, in the horizontal symmetry plane after 180 s – this work

the centre of the load (plane $z = 0$), even though the dielectric material was placed symmetrically with respect to the waveguide feed. In the vertical plane of symmetry (Figure 8), most of the heating takes place at the bottom right corner of the workload. The temperature in this region is very high compared to the temperatures in the centre.

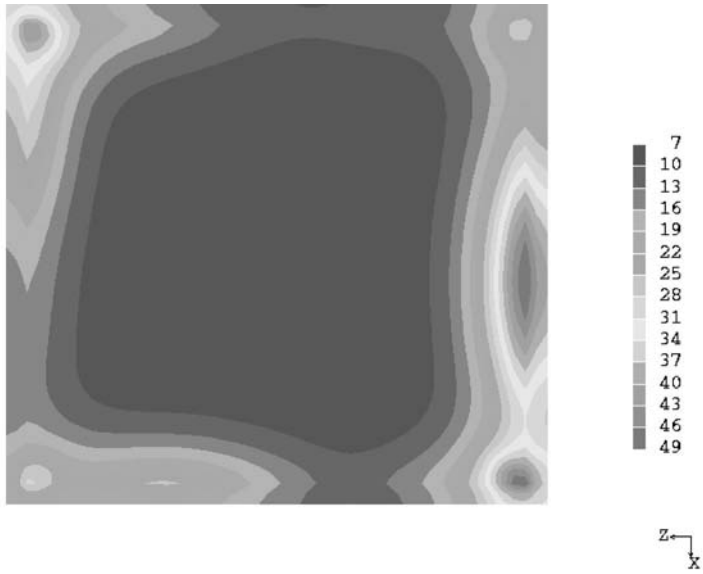

Figure 7.
Calculated temperature distribution, T(°C), in the horizontal symmetry plane after 180 s – this work

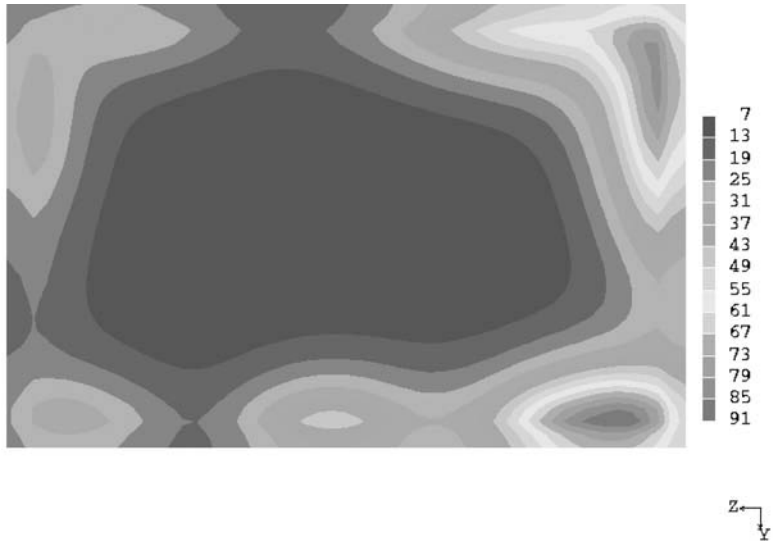

Figure 8.
Calculated temperature distribution, T(°C), in the vertical symmetry plane after 180 s – this work

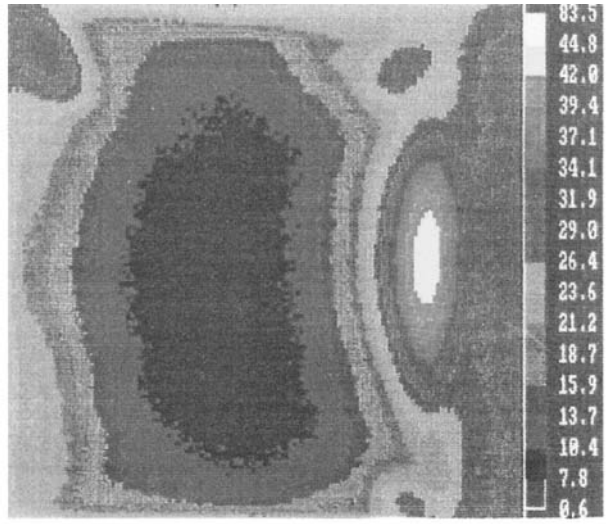

Source: DR. J. Bows (Ma *et al*. 1995)

Figure 9.
Measured temperature distribution, T(°C), in the horizontal plane after 180 s – experimental results

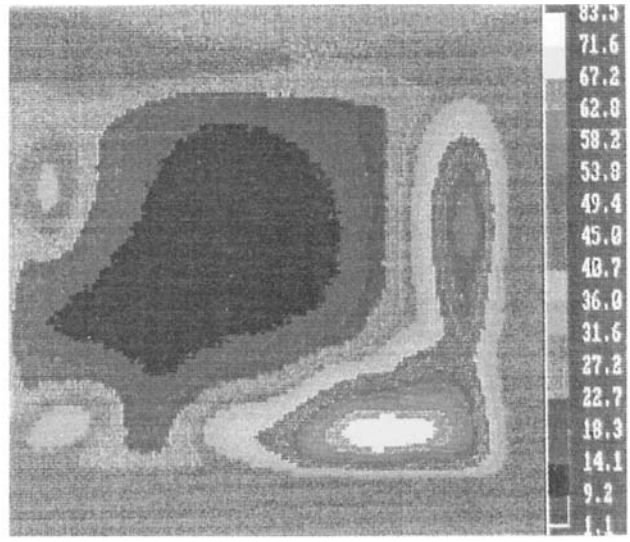

Source: DR. J. Bows (Ma *et al*. 1995)

Figure 10.
Measured temperature distribution, T(°C), in the vertical plane after 180 s – experimental results

8.1 Results and discussion

Computational results for the problem geometry and material properties described in the previous sections are shown in Figures 11-18. This problem definition was chosen to highlight the fundamental physical mechanisms involved in the microwave processing of porous bio-materials and is not intended to reflect commercial

applications. The software is however, sufficiently flexible to include features such as packaging when appropriate.

The results are presented as cross sections of the heated biomaterial showing the important physical variables – temperature (Figures 14 and 18), gas pressure (Figures 13 and 17), heat source Q (Figures 11 and 15), and liquid saturation (Figures 12 and 16) – at $t = 20$ and 150 s, and temperature histories at sample points in the interior and close to the top surface (Figure 19). The cross sections are in the y-z plane so that the excitation waveguide is on top (Figure 3) and are sampled approximately midway through the biomaterial. Since the biomaterial is not packaged moisture and heat can escape from all surfaces.

Figure 18 shows the calculated temperature distribution in the workload at the end of the simulated heating time. Most of the heating takes place on the corners of the biomaterial due to the local singularities at corners and edges of a lossy rectangular

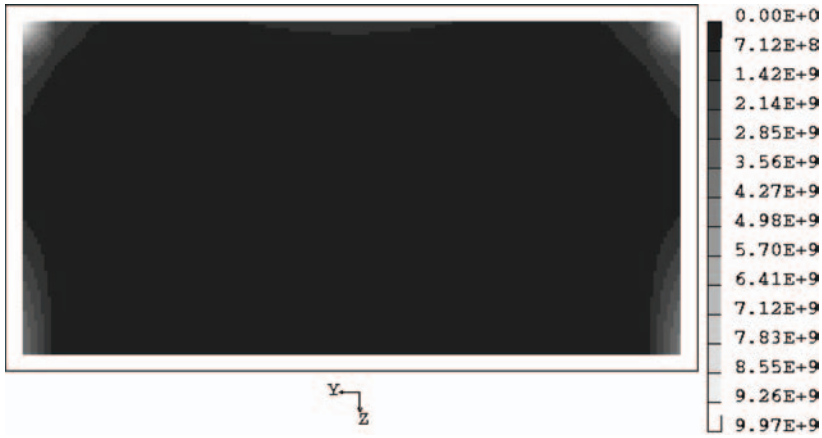

Figure 11.
Heating function, Q(W/m), inside the potato at $t = 20$ s

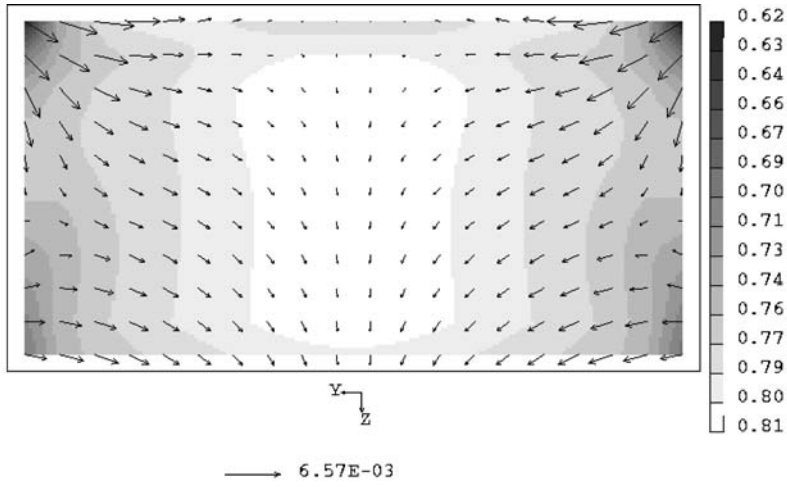

Figure 12.
Liquid saturation, S_w, inside the potato at $t = 20$ s

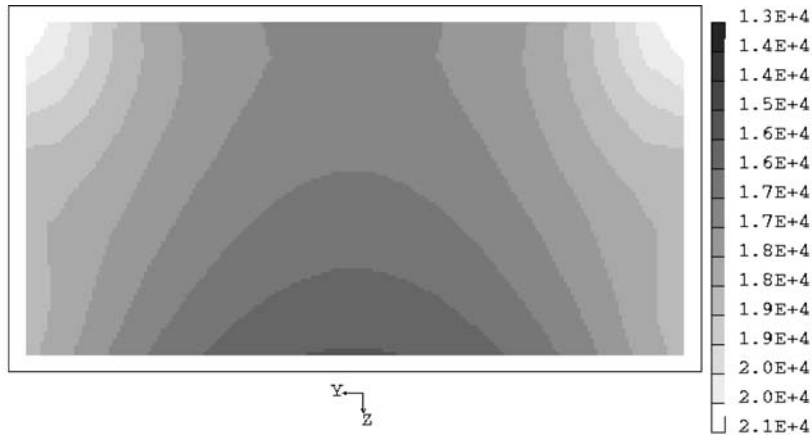

Figure 13.
Dynamic pressure profile, p(Pa), inside the potato at $t = 20$ s

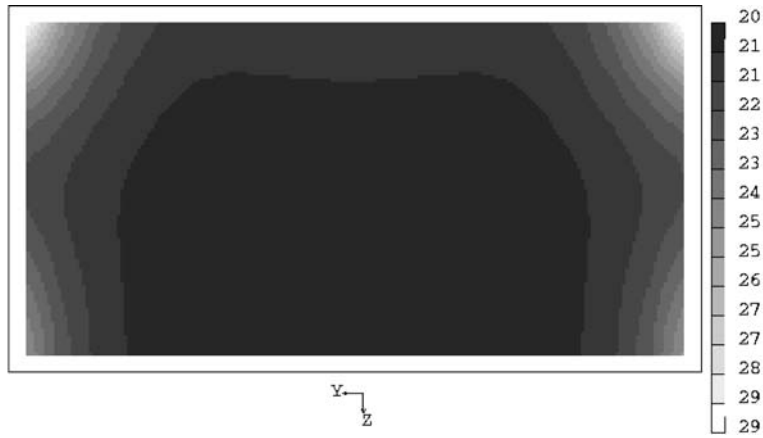

Figure 14.
Liquid temperature profile, T_l(°C), inside the potato at $t = 20$ s

dielectric. The temperatures at these points reached about 90°C. At the centre of the workload, the temperatures have increased to only about 30°C (Figure 19). Poor heating of the interior is mainly due to the low thermal conductivity of the load.

One important factor is that the power dissipation of the microwaves strongly depends on the moisture content of the material. As the moisture content decreases, the loss factor decreases, and consequently, the volumetric heating due to microwave power dissipation is reduced. Figures 13 and 17 show that due to the increase in temperature, the gas pressure increases around the localised heating areas driving a flow of liquid (Figure 16) away from these areas. As the moisture decreases and the temperature increases, the penetration depth will increase (Figure 4). It can be seen that for the moisture content of around 0.20 (Figure l6), the analytically obtained value of the penetration depth is approximately 2 cm. This is in agreement with the computationally obtained results shown in Figure 15. This phenomenon demonstrates the importance of coupling a fully multiphase porous media flow dynamics to the

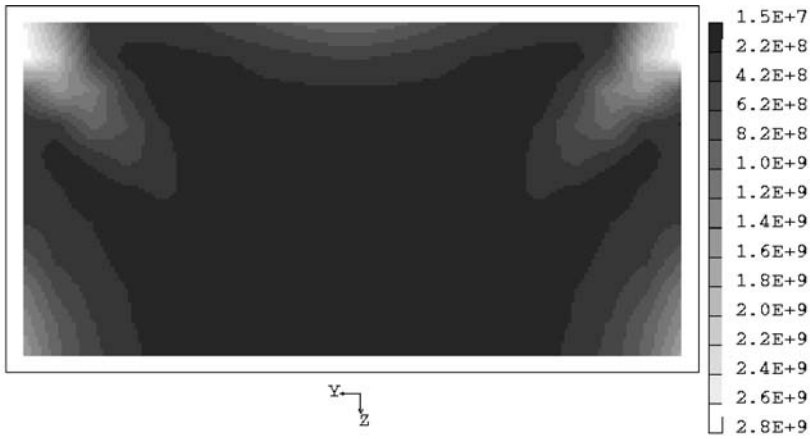

Figure 15.
Heating function, Q(W/m), inside the potato at $t = 150$ s

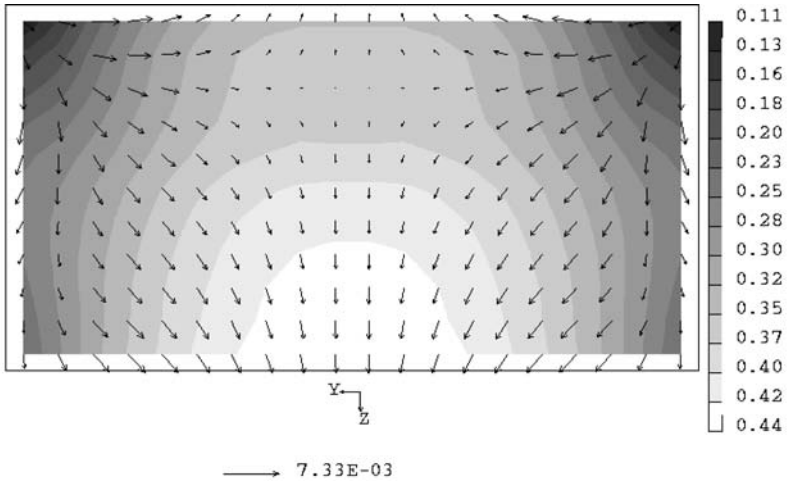

Figure 16.
Liquid saturation, S_w, inside the potato at $t = 150$ s

microwave heating. The mathematical model allows for evaporation (i.e. mass transfer between the liquid and gas phase) to take place within the porous material at all temperatures below the boiling point; the evaporation rate will be dependent on the surface area of the liquid phase which is in turn dependent on the porous structure. This parameter has been set to provide fairly rapid evaporation in this case, but would be need to be matched to the experimental measurements in a commercial application. Similar results are reported by Perré and Turner (1999) for timber drying (with higher internal pressure increases due to the lower permeability of timber) and Ni *et al.* (1999) in a one-dimensional model of a material with similar permeabilities reported internal pressure buildups of a similar magnitude.

These results took around 2 h to produce with around 24,000 electromagnetic grid cells and 4,000 finite volumes on a Sun Ultra5, 400 MHz CPU processor. Fine grid computations (not shown here) with 190,000 electromagnetic grid cells and 32,000 finite

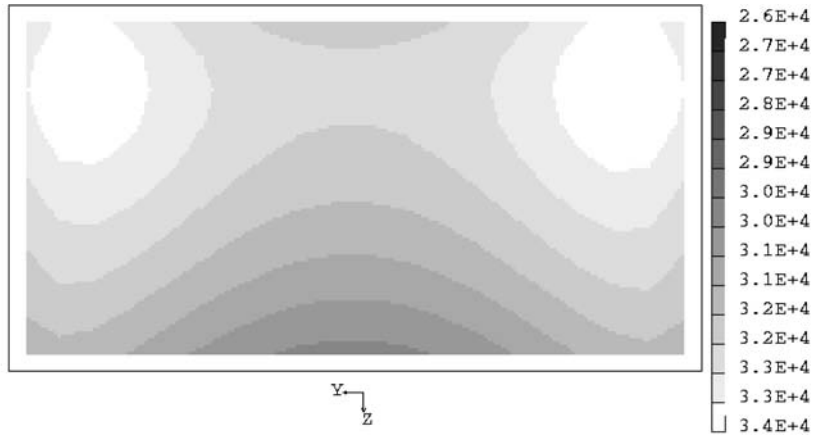

Figure 17.
Dynamic pressure profile, p(Pa), inside the potato at $t = 150$ s

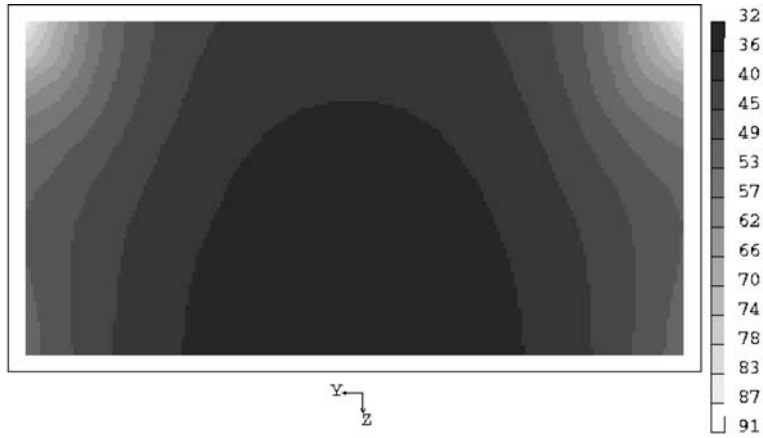

Figure 18.
Liquid temperature profile, T_l(°C), inside the potato at $t = 150$ s

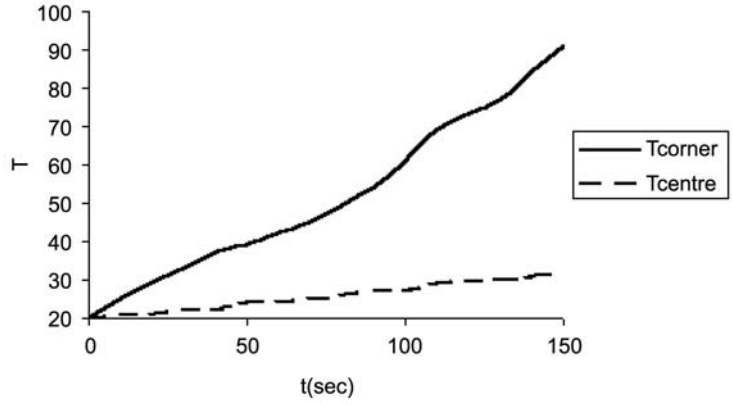

Figure 19.
Temperature, T(°C), evolution over time at two different points in cross section

volumes showed relatively small changes to the original calculations. These coupled computations are clearly expensive, but would run significantly faster on the latest Sun processors.

9. Conclusion

A multiphase transport model of a porous media, which combines a three-dimensional heat and mass transfer code with a three-dimensional electromagnetic computational scheme, was able to predict the overall drying behaviour. The two calculations have been closely coupled in an optimally cost-efficient manner. Temperature and moisture dependent dielectric properties were used. The model accounts for the pressure driven fluid flow and change of phase in wet bio-materials. Drying occurs due to liquid movement which does not occur during more conventional drying processes. The characteristics of heat and mass transfer are greatly influenced by internal heat generation. With the internal heat generation, most of the moisture is vapourized before leaving the sample. An agreement between calculated values for penetration depth and the distribution of the heating function inside the sample as dielectric properties change was achieved. This model can be used as a good basis for understanding coupled heat and mass transfer in a porous media under microwave heating.

References

Ayappa, K.G., Davis, H.T., Crapiste, G., Davis, E.A. and Gordon, J. (1991), "Microwave heating: an evaluation of power formulations", *Microwave Heating: An Evaluation of Power Formulations*, Vol. 46, pp. 1005-16.

Bear, J. (1998), *Dynamics of Fluids in Porous Media*, Dover Publications, New York, NY.

Bengtsson, N. and Ohlsson, T. (1974), "Microwave heating in the food industry", Proceedings of the IEEE, Vol. 62, pp. 44-54.

Chamchong, M. and Datta, A.K. (1999), "Thawing of food in a microwave oven. II. Effect of load geometry and dielectric properties", *Journal of Microwave Power and Electromagnetic Energy*, Vol. 34 No. 1, pp. 22-31.

Datta, A.K. and Anantheswaran, R.C. (2001), *Handbook of Microwave Technology for Food Applications*, Marcel Dekker, New York, NY.

Fu, W. and Metaxas, A. (1994), "Numerical prediction of three-dimensional power density distributions in a multi-mode cavity'", *Journal of Microwave Power and Electromagnetic Energy*, Vol. 29 No. 3, pp. 67-75.

Ishii, M. (1975), *Thermo-fluid Dynamic Theory of Two-phase Flow*, Eyrolles Book Publication.

Lyins, D.W. and Hatcher, J.D. (1972), "Drying of a porous medium with internal heat generation", *International Journal of Heat and Mass Transfer*, Vol. 15, pp. 897-905.

Ma, L., Paul, D-L., Pothecary, N., Railton, C., Bows, J., Barratt, L., Mulin, J. and Simons, D. (1995), "Experimental validation of a combined electromagnetic and thermal FTDT model of a microwave heating process", *IEEE Transactions on Microwave Theory and Techniques*, Vol. 43 No. 11, pp. 2565-72.

Metaxas, A.C. and Meredith, R.J. (1983), *Numerical Heat Transfer and Fluid Flow*, McGraw-Hill, London.

Monk, P. (1996), "Sub-gridding FTDT schemes", *ACES Journal*, Vol. 11, pp. 37-46.

Monk, P. and Parrott, K. (2001), "Phase-accuracy in comparisons and improved far field estimates for 3D edge element on tetrahedral meshes", *Journal of Computational Physics*, Vol. 170, pp. 614-43.

Monk, P. and Suli, E. (1994), "Error-estimate for Yee's method on non-uniform grids", *IEEE Transactions on Magnetics*, Vol. 30 No. 5, pp. 3200-3.

Ni, H., Datta, A.K. and Torrance, K.E. (1999), "Moisture transport in intensive microwave heating of biomaterials: a multiphase porous media model", *International Journal of Heat and Mass Transfer*, Vol. 42, pp. 1501-12.

Patankar, S.V. (1980), *Numerical Heat Transfer and Fluid Flow*, Hemisphere Publishing Corporation, New York, NY.

Perré, P. and Turner, I.W. (1999), "A 3D version of transpore: a comprehensive heat and mass transfer computational model for simulating the drying in porous media", *International Journal of Heat and Mass Transfer*, Vol. 42, pp. 4501-21.

PHOENICS code (2002), CHAM ltd Wimbledon, available at: www.cham.co.uk

Saltiel, G. and Datta, A.K. (1999), "Heat and mass transfer in microwave processing", *Advances in Heat Transfer*, Vol. 33 No. 1, pp. 1-94.

Spalding, D.B. (1981), "Numerical computation of multiphase flow and heat-transfer", *Recent Advances in Numerical Methods in Fluids*, Pineridge Press, Swansea.

Yee, K.S. (1966), "Numerical solution of initial boundary values problems involving Maxwell's equations in isotropic media", *IEEE Trans. Antennas Propag.*, Vol. 14, pp. 302-7.

Zheng, F., Chen, Z. and Zhang, J. (2000), "Toward the development of a three-dimensional unconditionally stable finite-difference time-domain method", *IEEE Transactions on Microwave Theory and Techniques*, Vol. 48 No. 9, pp. 1550-8.

Zhou, L., Puri, V.M., Anantheswaran, R.C. and Yeh, G. (1994), "Finite element modeling of heat and mass transfer in food materials during microwave heating – model development and validation", *Journal of Food Engineering*, Vol. 25 No. 9, pp. 509-29.

Živanovic, S., Yee, K.S. and Mei, K. (1991), "A subgridding method for the time-domain finite-difference method to solve maxwell's equations", *IEEE Transactions on Microwave Theory and Techniques*, Vol. 39 No. 3, pp. 471-9.